Virtual Inertia Design Procedure for Energy Storage Systems to Increase Frequency Response Performance in Microgrids

Gorn Suphahatthanukul†,
Pisitpol Chirapongsananurak, and **Naebboon Hoonchareon**, Non-members

ABSTRACT

The frequency instability caused by low system inertia is a common problem for small power systems such as microgrids since it can lead to stepping load shedding and generation tripping when disturbances occur. To alleviate the problem, this paper proposes a procedure for the virtual inertia design of an energy storage system (ESS) using the linear quadratic regulator (LQR) technique. The advantage of this proposed procedure is that it can separately manipulate the frequency response performance indices: the nadir and rate of change of frequency (RoCoF). The results confirm that the proposed procedure enables the microgrid to maintain frequency stability and avoid unnecessary load shedding whether operating in the grid-connected or islanding mode.

Keywords: Energy Storage System, Microgrid, Virtual Inertia, Frequency Response Performance

1. INTRODUCTION

In the present day, power systems in some areas have the potential to operate in the islanding mode because the amount of generated power is sufficient for meeting continuous electricity demand. However, the microgrid can often become unstable and insecure [1, 2] when operating in the islanding mode or unintentionally transitioning from grid-connected to islanding mode. For instance, a transient stability problem can occur as a result of large disturbances such as tie-line tripping, generator tripping, and immediate load shedding. Consequently, the system frequency can deviate from nominal during the transient period, and might violate the grid code and eventually trigger a frequency relay at the power plant to prevent damage to the mechanical parts of generation units. Once the frequency relays at the generation unit have been initiated, the power decreases further, causing the power system to deteriorate in terms of frequency stability. One of the causes of increased severity in transient stability is the low inertia situation resulting from the high PV penetration in the power system or a low synchronous machine rating when the microgrid is operating in the islanding mode [1].

There are several ways of alleviating this problem. Firstly, a synchronous condenser can be employed to provide sufficient inertia to power the system and has been used for some time in several countries. For example, Australian grid operators employ the synchronous condenser to keep the inertia level secure [3, 4]. It improves the system frequency and RoCoF as well as increasing the penetration level of renewable energy sources (RES). Another increasingly common option for maintaining system frequency stability is demand-side management which is used for thermostatically controlled loads such as in air conditioners and refrigerators. As a result, when the generated power decreases unintentionally, these loads can decrease their consumption rate to balance the power. According to previous research carried out in Great Britain, this method could reduce the RoCoF [5]. Moreover, batteries and ultra-capacitors, mostly connected to systems via an inverter, have recently become a popular energy storage, which could increase the power response performance if properly controlled. Other researchers used a combination of equipment for the efficient management of the power imbalance [6–8]. The reason for combining components is that the use of a battery alone could subject it to stress, while the combined method can reduce such stress and increase battery life [9].

There are various control patterns in an inverter-based generation unit and these can roughly be divided into five forms. The first pattern, namely the inducverter [10], mimics induction machine behavior. The plus point is that the inducverter can self-start and automatically synchronize, without the use of other devices. The second pattern is dubbed the synchroverter. It is an inverter which emulates the total synchronous machine characteristics including

Manuscript received on October 15, 2020 ; revised on February 15, 2021 ; accepted on April 19, 2021. This paper was recommended by Associate Editor Matheepot Phattanasak.

The authors are with the Smart Grid Research Unit, Department of Electrical Engineering, Faculty of Engineering, Chulalongkorn University, Bangkok, Thailand.

†Corresponding author: gorn.sup@hotmail.com

Digital Object Identifier 10.37936/ecti-eec.2021193.242211

the swing equation to provide inertia to the system [11, 12]. However, due to the complexity of the equations used to control the inverter, significant computational effort is required, causing software instability in some cases. Thirdly, the virtual synchronous machine (VISMA) is controlled by using the fifth-order synchronous generator model [13] while [14, 15] use the seventh-order model. The VISMA can operate in both grid-connected and islanded modes [16], while also providing inertial response to the system when power mismatch occurs. The fourth pattern is VSYNCH's VSG [13]. This algorithm uses a phase-lock-loop block, which may adversely affect performance, and uses energy storage to mimic inertia to the system [17]. Lastly, [18, 19] use the droop equation to control inverters in response to frequency deviation.

This paper proposes a state-of-the-art method to connect ESS to the power system via inverters with the desired dynamic behavior to increase the frequency response performance using the linear quadratic regulator (LQR) technique, commonly known as adaptive virtual inertia. The advantage of this method is that it is simple and practical to implement in a real microgrid without needing significant computational effort and system modification. Moreover, this method offers freedom in terms of controlling frequency deviation and the RoCoF individually. In some power systems, depending on the components involved, the nadir frequency may not violate the frequency standard but RoCoF exceeds the limit. In contrast to the proposed methods, inverters controlled by constant inertia cannot deliberately reduce the only one index that exceeds the limit. The proposed method is also easy to implement and can guarantee stability during transient conditions.

This paper is outlined as follows: Section 2 presents the fundamental knowledge, while the controller design using the LQR technique and implementation procedure is elaborated in Sections 3 and 4, respectively. The test system parameter and procedure are described in Section 5, while the results are detailed in Section 6. Finally, Sections 7 and 8 present the sensitivity analysis and conclusion, respectively.

2. FUNDAMENTAL KNOWLEDGE

This section describes the control process of the ESS to the moment of inertia. The LQR technique is then introduced and the frequency response performance indices described.

2.1 VIRTUAL INERTIA

In each synchronous generator, the moment of inertia is inherent because it involves a rotating part. The moment of inertia is one of the most important factors in helping the power system respond to frequency deviation when disturbances occur. Specifically, it represents the ability of the power system to resist any changes in frequency. The following swing equation describes the behavior of the rotor:

Fig. 1: *ESS dynamic model.*

$$\frac{2H}{\omega_s}\frac{d\Delta\omega}{dt} = P_m - P_e \tag{1}$$

where H denotes the inertia constant of both turbine and generator, ω_s denotes synchronous angular velocity, $\Delta\omega$ is the relative angular velocity, P_m and P_e signify the mechanical power and electrical power in each unit, respectively.

Due to the high penetration present in renewable energy power plants, they do not usually respond to frequency deviation, resulting in frequency response performance impairment. This is because these power plants are connected to the power system by inverters, which have no moment of inertia. It should be noted that this assumption is based on the situation that synchronous generators are replaced by PV plants. Therefore, researchers attempt to create some degree of inertia in non-intrinsic-inertia generators to increase the frequency response performance. For instance, the swing equation can be modified slightly to make it suitable for ESS application as follows:

$$\Delta P_{ESS} = -2H_{ESS}\frac{d\Delta\omega}{dt} \tag{2}$$

where H_{ESS} signifies the virtual moment of ESS inertia, ΔP_{ESS} is the ESS power deviation during a disturbance period, and $\Delta\omega$ denotes system frequency deviation. Fig. 1 presents a dynamic model for ESS.

2.2 Linear Quadratic Regulator Technique

The LQR technique is a negative feedback control method, representing a trade-off between the relative importance of error and expenditure in controlling energy use. Fig. 2 shows the model used in this technique. The objective function of the LQR method is [20]:

$$\min J = \int_0^\infty x^T Q x + u^T R u \; dt \tag{3}$$

whereas the constraint equations are

$$\dot{x} = Ax + Bu \tag{4}$$

$$u = -Kx \tag{5}$$

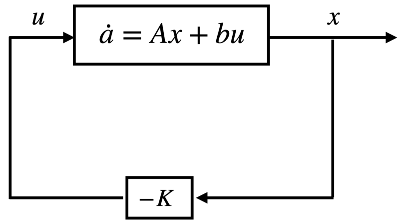

Fig. 2: *Negative feedback control scheme.*

This technique represents a trade-off between states and expenditure by adjusting the state-cost weighted matrix (Q) and input-cost weighted matrix (R); the dimensions of which depend on state space. The dimension of matrix Q equals the dimension of the dynamic matrix (A), and is the positive definite, whereas the dimension of matrix R equals the dimension of the input matrix (B).

The output of this technique is optimal gain (K) corresponding to matrices Q and R. There are two steps to obtaining matrix K. Firstly, matrix P is solved from a reduced-matrix Riccati equation, as follows:

$$A^T P + PA - PBR^{-1}B^T P + Q = 0 \tag{6}$$

Matrix K will subsequently be solved from

$$K = R^{-1}B^T P \tag{7}$$

2.3 Frequency Response Performance Indices

When disturbances occur, the system frequency deviates from the nominal level, which might trigger the frequency protection system at the power plant. The objective of frequency protection for synchronous generators in power plants is to prevent them and their prime mover from being damaged. For instance, the synchronous generator may be subject to over-fluxing while operating outside the nominal speed, causing mechanical damage to the turbine and generator bearings, while a low steam flow rate in the turbine may lead to a hot spot on the near-last state turbine blades. The most popular criteria for achieving frequency relay are the nadir frequency and RoCoF. Therefore, these criteria are chosen as the frequency response performance indices in this paper. However, the criteria are different depending on the country or standard involved. For instance, according to the System Performance Under Single Contingency Standard of the Electricity Generating Authority of Thailand (EGAT) [21], the frequency deviation should be less than ±0.5 Hz, and this is therefore used as the criterion in this paper.

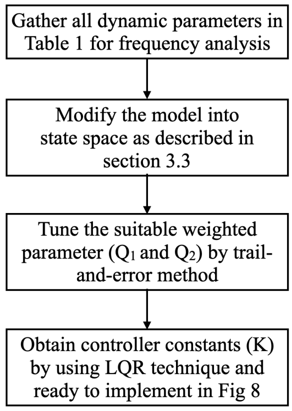

Fig. 3: *Flow chart controller design procedure.*

3. CONTROLLER DESIGN USING THE LQR TECHNIQUE

3.1 Procedure Overview

This section describes the procedure for designing the optimal gain (K) of the ESS controller in the microgrid using the LQR technique. Fig. 3 presents a simple flow chart of the procedure which starts with the gathering of all dynamic parameters of each system component. To maintain microgrid frequency stability at all times, the disturbance ΔP_L, could represent any of the following: the maximum power in the tie-line before the disturbance occurs, the maximum power of the biggest generator-tripping contingency, or the loss of the largest load when a short-circuit fault occurs in a feeder. The procedure then follows the ensuing sections in order.

3.2 Test System Components and the Dynamic Model

Several tools can be used to study transient stability and result verification, but this paper uses the time-domain simulation method. The results can be used to analyze system stability without significant computational effort. However, to obtain accurate results, the dynamic model used in the simulation should firstly reflect the exact behavior of the power system. Due to the rapid increase in PV generation in Thailand and its low wind power production potential, the test system in this paper consists of a group of synchronous generators, PV power plants, an energy storage system, and a lumped load as demonstrated by the microgrid scheme in Fig. 4. This microgrid is connected to the main grid via a tie-line.

The simplified dynamic model suitable for studying the frequency stability of the system in Fig. 4 is shown in Fig. 5. The model represents all vital components in this test system consisting of the synchronous generator, turbine, governor, and the mechanism for regulating system frequency. H_{sys} and D_{sys} are the lumped inertia and damping coefficient

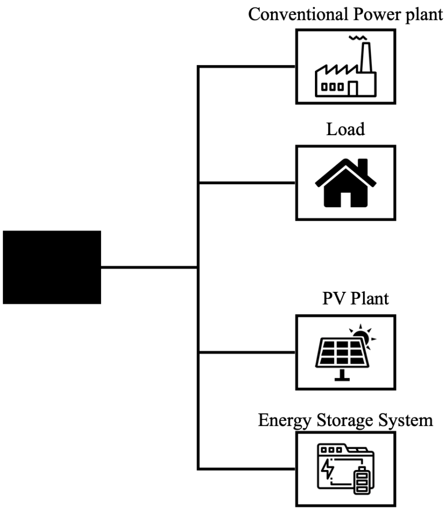

Fig. 4: *Single line diagram.*

of the system, respectively. R_{sys} is the droop constant of the governor, while T_1 and T_2 represent the turbine and governor time constants, respectively. It should be noted that this model ignores the dead-band in the governor and does not yet include the model of ESS.

The primary and secondary responses regulate the system frequency in the power system. The objective of the former is to halt system frequency deviation. The parameters relating to the primary response performance are mainly the system inertia and droop constant of each governor. The objective of the latter is to bring the deviated system frequency back to the nominal level by changing the real power reference signal of each generator from the control center. However, in this paper, the secondary response to frequency deviation is neglected because it focuses on the effect of the primary response parameters, especially system inertia.

To ensure the dynamic model shown in Fig. 5 represents the power system (comprising conventional generators and ESS), the simplified model of ESS is added as presented in Fig. 6. The dynamic model of ESS is described in [22], and depends on a dominated time constant in the control loop, which in this paper is T_{ESS}, and the time delay of ESS. H_{ESS} signifies the virtual inertia constant of ESS while D_{ESS} is the virtual damping coefficient of ESS. It should be noted that the time constants of the turbine and governor, namely T_1 and T_2, are combined to produce T.

3.3 Mathematical Model for the LQR Technique and Linearization [23]

It is clear that the application of the LQR technique to control the virtual inertia of ESS, according to the mathematical model in Fig. 6, must be rearranged into a state-space representation. The transfer function of the simplified model in Fig. 6 can

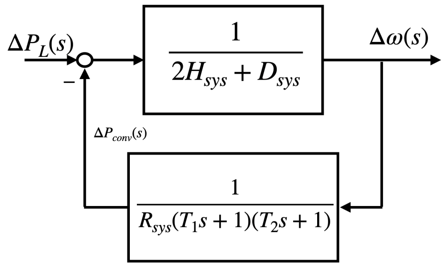

Fig. 5: *Conventional dynamic model.*

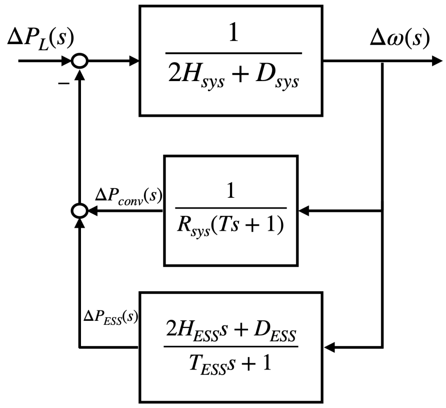

Fig. 6: *Dynamic model for the controller design.*

be written as

$$F(s) = \frac{\Delta\omega(s)}{\Delta P_L(s)} = \frac{R_{sys}Ts + 1}{R_{sys}\widetilde{H}Ts^2 + R_{sys}\left(\widetilde{H} + T\right)s + R_{sys}\widetilde{D} + 1} \tag{8}$$

where

$$\widetilde{H} = H_{sys} + H_{ESS} \tag{9}$$

$$\widetilde{D} = D_{sys} + D_{ESS} \tag{10}$$

Therefore, the state-space representation of the model is

$$\begin{bmatrix} \dot{\omega} \\ \ddot{\omega} \end{bmatrix} = \begin{bmatrix} 0 & 1 \\ -\dfrac{R_{sys}\widetilde{D} + 1}{R_{sys}\widetilde{H}T} & -\dfrac{\widetilde{H} + T}{\widetilde{H}T} \end{bmatrix} \begin{bmatrix} \omega \\ \dot{\omega} \end{bmatrix} + \begin{bmatrix} 0 \\ \dfrac{\Delta P_L}{\widetilde{H}T} \end{bmatrix} \tag{11}$$

$$y = \begin{bmatrix} 1 & 0 \\ 0 & 1 \end{bmatrix} \begin{bmatrix} \omega \\ \dot{\omega} \end{bmatrix} \tag{12}$$

Using the LQR technique to control the virtual inertia of ESS, the control input (u) is selected as

$$u = \Delta\widetilde{H} = \widetilde{H} - \widetilde{H}_0 = -\begin{bmatrix} K_1 & K_2 \end{bmatrix} \begin{bmatrix} \omega \\ \dot{\omega} \end{bmatrix} \tag{13}$$

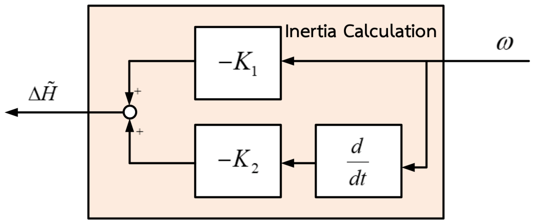

Fig. 7: *Inertia calculation block diagram.*

Consequently, the equations representing the micro-grid system become nonlinear and must be linearized as

$$\begin{bmatrix}\Delta\dot{\omega}\\ \Delta\ddot{\omega}\end{bmatrix} = \begin{bmatrix}0 & 1\\ -\dfrac{R_{sys}\widetilde{D}_0+1}{R_{sys}\widetilde{H}_0T} & -\dfrac{\widetilde{H}_0+T}{\widetilde{H}_0T}\end{bmatrix}\begin{bmatrix}\Delta\omega\\ \Delta\dot{\omega}\end{bmatrix} + \begin{bmatrix}0\\ \dfrac{\Delta P_L}{\widetilde{H}_0^2T}\end{bmatrix}\Delta\widetilde{H} \tag{14}$$

where $\widetilde{H}_0$ is the total system inertia comprising the synchronous machine inertia and the virtual inertia from ESS before the disturbances occur, $\widetilde{D}_0$ is the total system damping coefficient comprising the synchronous machine damping and the virtual damping from ESS before the disturbances occur.

3.4 Weighted Parameters

The weight-parameter group is used in the LQR technique, imposed as matrices Q and R. According to Eqs. (13) and (14), these matrices can be written as

$$Q = \begin{bmatrix}Q_1 & 0\\ 0 & Q_2\end{bmatrix} \tag{15}$$

$$R = [R_1] \tag{16}$$

According to Eq. (3), it is noticeable that Q_1, Q_2, and R_1 independently affect $\Delta\omega$, $\Delta\dot{\omega}$, and $\Delta\widetilde{H}$, respectively. Therefore, it should be noted that the values of each weighted parameter are related to each other in terms of proportion. There are various methods for imposing these weighted parameters to achieve the desired system performance, but this paper uses the trial-and-error method.

4. IMPLEMENTATION PROCEDURE

So far, the matrix K is achieved using the LQR technique. Fig. 7 presents a block diagram demonstrating the method for calculating ESS inertia according to Eq. (13). The input of the block diagram is the angular velocity while the output is the change in ESS inertia. The parameters K_1 and K_2 represent the elements of matrix K. The adaptive virtual inertia of ESS in Eq. (2) is therefore modified for implementation as

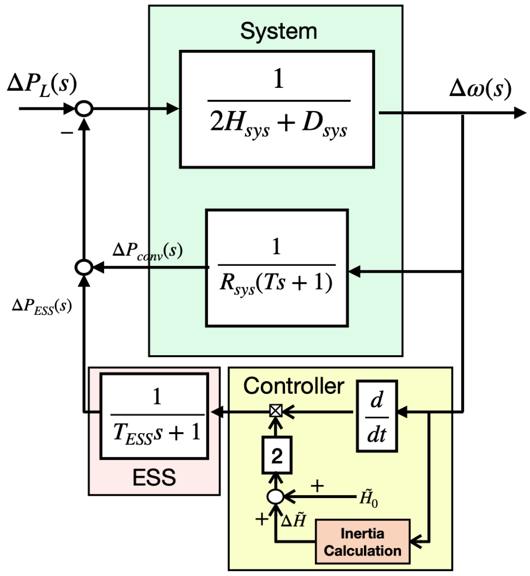

Fig. 8: *Complete dynamic model.*

$$\Delta P_{ESS} = -2\left(\widetilde{H}_0 + \Delta\widetilde{H}\right)\frac{d\Delta\omega}{dt} \tag{17}$$

Fig. 8 shows the complete dynamic model after inclusion of the adaptive virtual inertia. The total ESS inertia is the signal from the inertia calculation block diagram combined with the initial ESS inertia proposed in Eq. (17). The value of each parameter in Fig. 8 are subsequently described in Sections 5.1 and 5.2.

It can be observed that this model is incredibly simple and practical to implement on a real micro-grid. The adaptive virtual inertia can guarantee that frequency stability and security is maintained in the microgrid, whether operating in a grid-connected or islanding mode. However, since governors of synchronous generators in each microgrid system are multifarious, the time constants of the governor and turbine in the dynamic model should be selected corresponding to their behavior.

5. TEST SYSTEM PARAMETER AND PROCEDURE

5.1 Test System Parameter

All main components are described superficially to formulate an accurate dynamic control model. In this section, all related parameters of those components in the microgrid test system shown in Fig. 4 are presented in detail. Firstly, the system base is selected as 10 MVA. The maximum load demand in this microgrid is 10 MW and the installation capacity of the PV power plant is 10 MW. There are two synchronous generators in this microgrid and the

Table 1: *Test system parameters.*

Parameter	Value
Inertia of Generator 1 (H_1)	5 s
Inertia of Generator 2 (H_2)	5 s
Damping Coefficient of Generator 1 (D_1)	0
Damping Coefficient of Generator 2 (D_2)	0
Droop Constant of Generator 1 (R_1)	0.05
Droop Constant of Generator 2 (R_2)	0.05
Initial Inertia of ESS (H_0)	0 s
Turbine Time Constant (T_t)	0.2 s
Governor Time Constant (T_G)	0.3 s
ESS Time Constant (T_{ESS})	0.01 s

Table 2: *Test system parameter for Case 1.*

Component	Real Power (MW)
Synchronous Generator 1	1.25
Synchronous Generator 2	1.25
PV Plant	6
Tie-Line	1.5 (Import)
Load Demand	10

Table 3: *Test system parameter for Case 2.*

Component	Real Power (MW)
Synchronous Generator 1	1.25
Synchronous Generator 2	1.25
PV Plant	9
Tie-Line	1.5 (Export)
Load Demand	10

rating of each is 5 MVA. The moment of inertia, damping coefficient, and droop constant of each generator are 5 s, 0, and 0.05, respectively. It should be noted that the three parameters are based on their machine rating. The time constants of the turbine, governor, and ESS are 0.2, 0.3, and 0.01 s, respectively. All parameters are presented in Table 1.

5.2 Test Procedure

This paper demonstrates the performance of the proposed method using three case studies, each with different disturbance patterns: tie-line tripping while importing real power into the microgrid, tie-line tripping while exporting real power to the main grid, and generation tripping while operating in the islanding mode. Although the uncertainties caused by the variation in renewable power generation is one form of disturbance, these are generally small compared to those described above.

In Case 1, the disturbance is tie-line tripping caused by a fault on the tie-line while importing real power into the microgrid, meaning that the microgrid is transferring from the grid-connected to the islanding mode. The operating point of all components prior to the disturbance is shown in

Table 4: *Test system parameter for Case 3.*

Component	Real Power (MW)
Synchronous Generator 1	2
Synchronous Generator 2	2
PV Plant	9
Tie-Line	3 (Export)
Load Demand	10

Table 5: *Test system parameter for Case 4.*

Component	Real Power (MW)
Synchronous Generator 1	1
Synchronous Generator 2	1
PV Plant	8
Load Demand	10

Table 2.

Matrices A and B in Eq. (11) represent the dynamic system used for calculating the control parameter in Case 1 as

$$A = \begin{bmatrix} 0 & 1 \\ -8 & -2.2 \end{bmatrix} \tag{18}$$

$$B = \begin{bmatrix} 0 \\ -0.06 \end{bmatrix} \tag{19}$$

In Case 2, the disturbance is tie-line tripping when exporting real power to the main grid, which results from exceeding the real power from the PV plant. The cause of tripping is the same as in Case 1. The operating point of all components prior to the disturbance is shown in Table 3. Since the difference between Cases 1 and 2 is the sign of the disturbances, matrices A and B in Eq. (11) remain the same as in Case 1.

In Case 3, the disturbance is also tie-line tripping. The operating point is similar to Case 1 except that the power from each synchronous generator increases from 1.25 to 2 MW. As a result, the tie-line power is 3 MW in the export direction. Table 4 displays all the operating points in Case 3.

Matrices A and B in Eq. (11) represent the dynamic system used for calculating the control parameter in Case 3 as

$$A = \begin{bmatrix} 0 & 1 \\ -8 & -2.2 \end{bmatrix} \tag{20}$$

$$B = \begin{bmatrix} 0 \\ 0.12 \end{bmatrix} \tag{21}$$

In Case 4, the disturbance is generator tripping when operating in the islanding mode. In this case, the conventional moment of inertia decreases to half that in Case 3. This is because only one machine provides the moment of inertia and primary response to the frequency deviation. The operating point of all components prior to the disturbance is shown in Table 5.

Matrices A and B in Eq. (11) represent the dynamic system used for calculating the control parameter in Case 4 as

$$A = \begin{bmatrix} 0 & 1 \\ -16 & -2.4 \end{bmatrix} \quad (22)$$

$$B = \begin{bmatrix} 0 \\ -0.08 \end{bmatrix} \quad (23)$$

The weighted parameters are different in each, depending mainly on the disturbance severity and dynamic system parameters. They are adjusted until the system frequency and RoCoF meet the system frequency standard. Moreover, since the generator inertia is generally based on its machine rating, the system inertia (H_{sys}) must be computed as well as the system droop constant (R_{sys}). In the realistic microgrids, the most severe disturbance should be used to guarantee that the microgrid can operate seamlessly in both grid-connected and islanded modes.

6. RESULTS

In each case, the disturbances occur at 1 s and consist of three subcases: 1) without virtual inertia, 2) the LQR technique with only Q_1 tuned, and 3) the LQR technique with both Q_1 and Q_2 tuned. Specifically, in the subcase without the virtual inertia, the ESS does not respond to the system frequency deviation (the Base Case), while the LQR technique with only Q_1 tuned refers to the subcase where only the weighted parameter Q_1 is adjusted and Q_2 is fixed (Subcase 1), and the LQR technique with both Q_1 and Q_2 tuned refers to the subcase where both weighted parameters are tuned (Subcase 2).

6.1 Case 1

The weighted parameters Q_1 and Q_2 are selected as 800,000 and 100,000, respectively. Accordingly, the optimal gains K_1 and K_2, as the output parameters of the LQR technique, for Subcase 1 are −448.88 and −145.94, whereas the optimal gains K_1 and K_2 for Subcase 2 are −448.88 and −273.20. Fig. 9 shows the frequency deviation during the disturbance period. The nadir frequencies for the Base Case, Subcase 1, and Subcase 2 are −0.5866, −0.4602, and −0.4506 Hz, respectively. Fig. 10 illustrates the RoCoF, for which the maximum values are −0.73, −0.5644, and −0.4838 Hz/s for the Base Case, Subcase 1, and Subcase 2, respectively. Fig. 11 depicts the ESS power when responding to the frequency deviation. The maximum power is 604 kW and energy used can be calculated as 11.75 kWh. The power from both synchronous generators is plotted in Fig. 12, while Fig. 13 shows the PV power, and Fig. 14 the adaptive ESS inertia.

6.2 Case 2

The weighted parameters Q_1 and Q_2 are selected as 800,000 and 100,000, respectively. Accordingly, the optimal gains K_1 and K_2 for Subcase 1 are 448.88 and 145.94, whereas the optimal gains K_1 and K_2 for Subcase 2 are 448.88 and 273.20. Fig. 15 shows the frequency deviation during the disturbance period. The nadir frequencies for the Base Case, Subcase 1, and Subcase 2 are 0.5866, 0.4602, and 0.4506 Hz, respectively. Fig. 16 illustrates the RoCoF, for which the maximum values are 0.73, 0.5644, and 0.4838 Hz/s for the Base Case, Subcase 1, and Subcase 2, respectively. Fig. 17 depicts the ESS power in response to the frequency deviation. The maximum power is 604 kW and the absorbed energy can be calculated as 11.75 kWh. The power from both synchronous generators is plotted in Fig. 18, while Fig. 19 shows the PV Power and Fig. 20 the adaptive ESS inertia.

6.3 Case 3

The weighted parameters Q_1 and Q_2 are selected as 800,000 and 100,000, respectively. Accordingly, the optimal gains K_1 and K_2 for Subcase 1 are 621.18 and 153.62, whereas the optimal gains K_1 and K_2 for Subcase 2 are 621.18 and 308.54. Fig. 21 shows the frequency deviation during the disturbance period. The nadir frequencies for the Base Case, Subcase 1, and Subcase 2 are 1.172, 0.802, and 0.792 Hz, respectively. Fig. 22 illustrates the RoCoF, for which the maximum values are 1.5, 0.94, and 0.7765 Hz/s for the Base Case, Subcase 1, and Subcase 2, respectively. Fig. 23 depicts the ESS power in response to the frequency deviation. The maximum power is 1.661 MW and the absorbed energy can be calculated as 12.86 kWh. The power from both synchronous generators is plotted in Fig. 24, while Fig. 25 shows the PV power and Fig. 26 the adaptive ESS inertia.

6.4 Case 4

The weighted parameters Q_1 and Q_2 are selected as 800,000 and 100,000, respectively. Accordingly, the optimal gains K_1 and K_2 for Subcase 1 are −724.74 and −150.66, whereas the optimal gains K_1 and K_2 for Subcase 2 are −724.74 and −313.48. Fig. 27 shows the frequency deviation during the disturbance period. The nadir frequencies for the Base Case, Subcase 1, and Subcase 2 are 0.5866, 0.5211, and 0.5108 Hz, respectively. Fig. 28 illustrates the RoCoF, for which the maximum values are 0.998, 0.6007, and 0.4723 Hz/s for the Base Case, Subcase 1, and Subcase 2, respectively. Fig. 29 depicts the ESS power in response to the frequency deviation. The

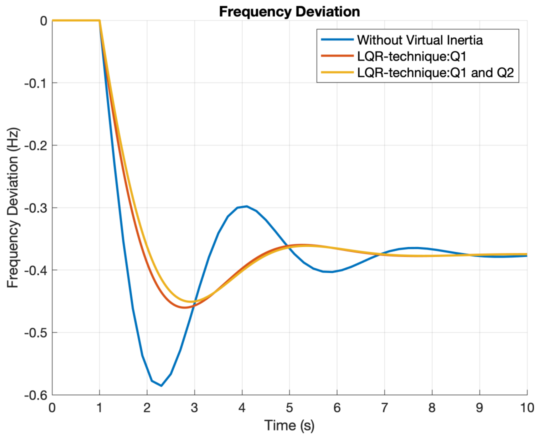

Fig. 9: *Frequency deviation for Case 1.*

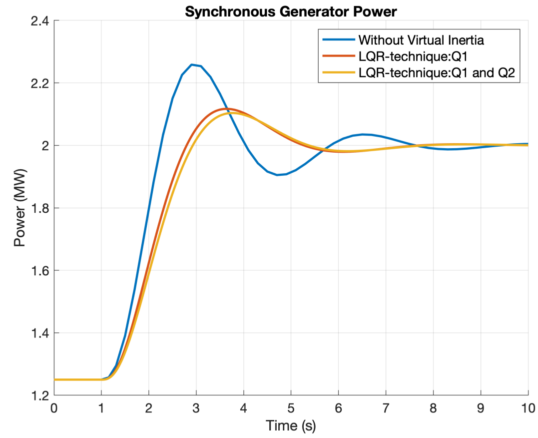

Fig. 12: *SG power #1 and #2 for Case 1.*

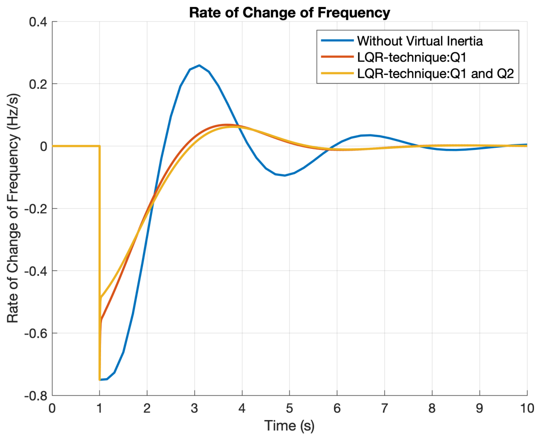

Fig. 10: *RoCoF for Case 1.*

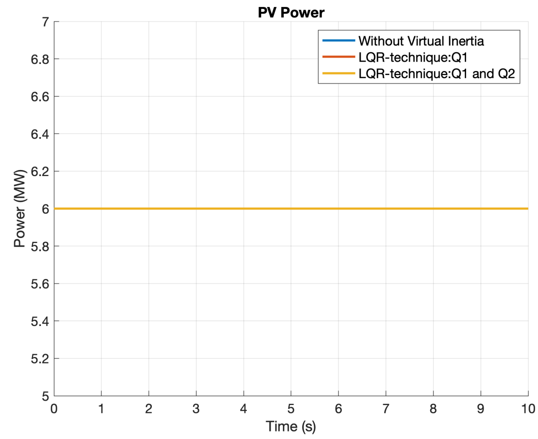

Fig. 13: *PV power for Case 1.*

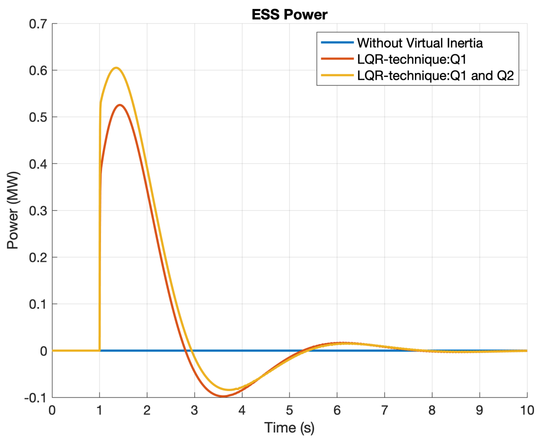

Fig. 11: *ESS power for Case 1.*

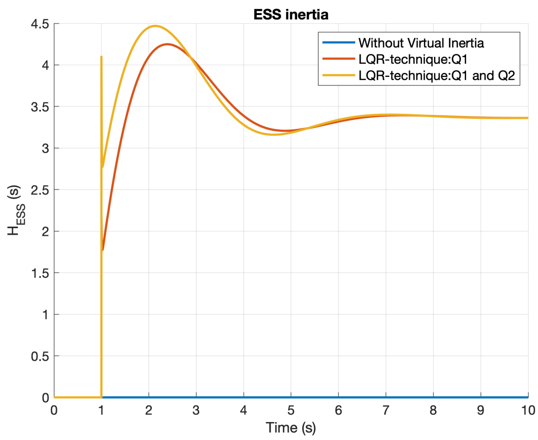

Fig. 14: *ESS inertia for Case 1.*

maximum power is 585 kW and the energy used can be calculated as 14.23 kWh. The power from both synchronous generators is plotted in Fig. 30, while Fig. 31 shows the PV power and Fig. 32 the adaptive ESS inertia. The power through tie-line is always 0 MW as shown in Fig. 33.

6.5 Discussion

It can immediately be observed that the nadir frequency and RoCoF of the system with the ESS controlled by the LQR technique are less than those of the system without the virtual inertia when

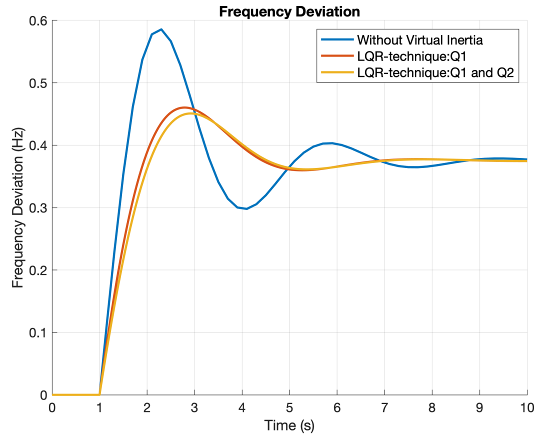

Fig. 15: *Frequency deviation for Case 2.*

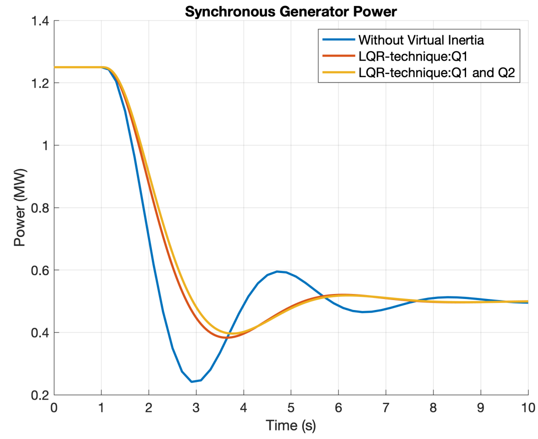

Fig. 18: *SG power #1 and #2 for Case 2.*

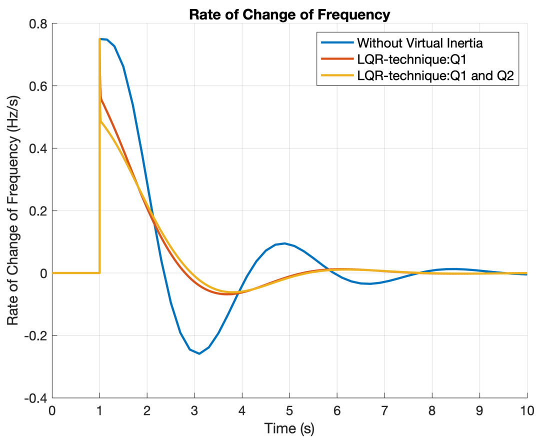

Fig. 16: *RoCoF for Case 2.*

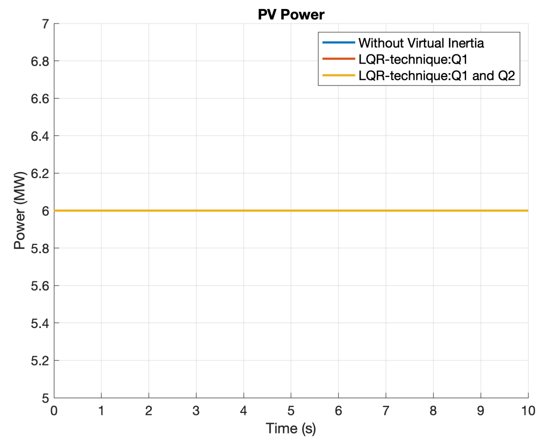

Fig. 19: *PV power for Case 2.*

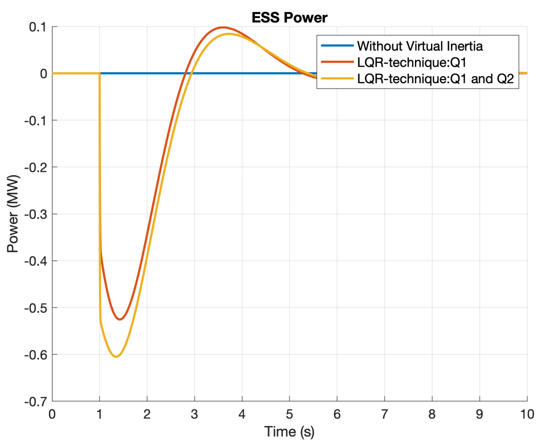

Fig. 17: *ESS power for Case 2.*

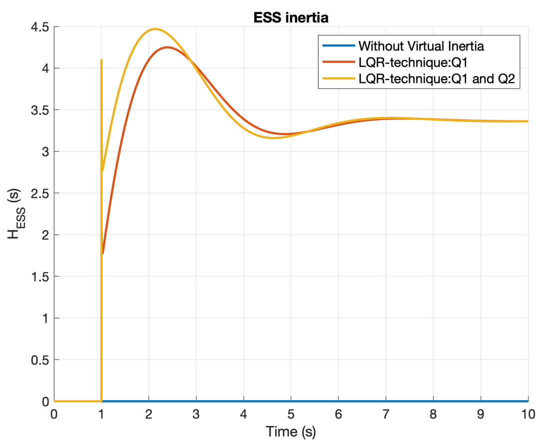

Fig. 20: *ESS inertia for Case 2.*

disturbances occur. Therefore, it could be said that the ESS controlled by the LQR technique helps the system to increase its frequency response performance in both grid-connected and islanding modes. Moreover, in the case where the ESS is controlled by the LQR technique, the weighted parameter could be adjusted independently. According to Section 3.4, the weighted parameter Q_1 relates to the frequency deviation, whereas Q_2 relates to the RoCoF. In addition, remarkably, although the weighted parameter Q_1 in Subcase 2 is equal to that in Subcase 1, the nadir frequency of Subcase 2 is lower

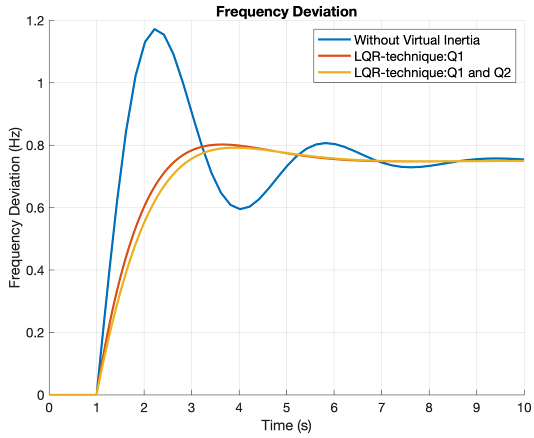

Fig. 21: *Frequency deviation for Case 3.*

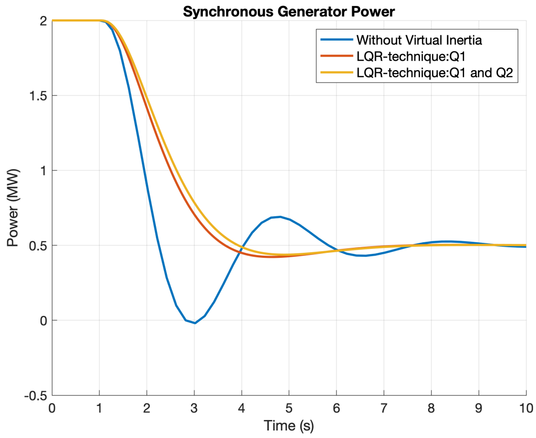

Fig. 24: *SG power #1 and #2 for Case 3.*

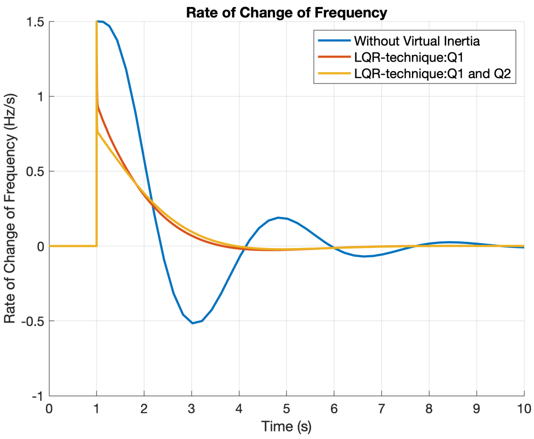

Fig. 22: *RoCoF for Case 3.*

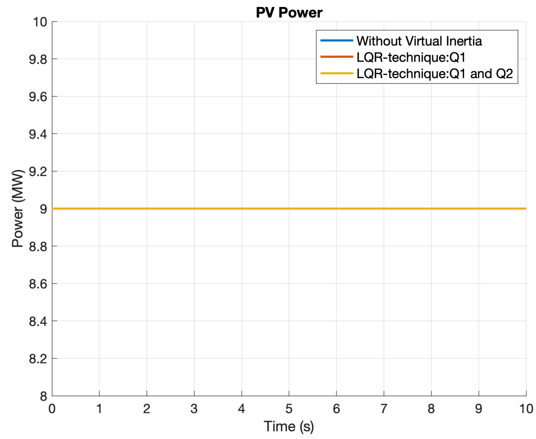

Fig. 25: *PV power for Case 3.*

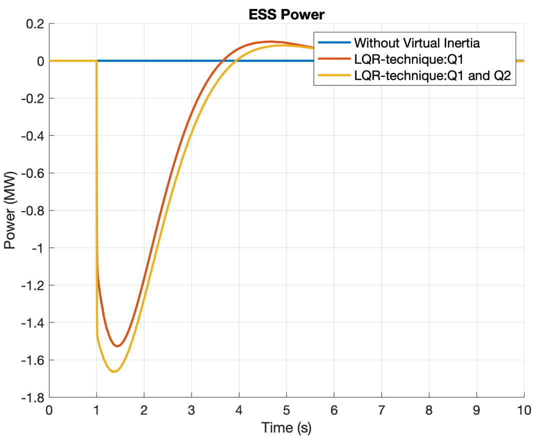

Fig. 23: *ESS power for Case 3.*

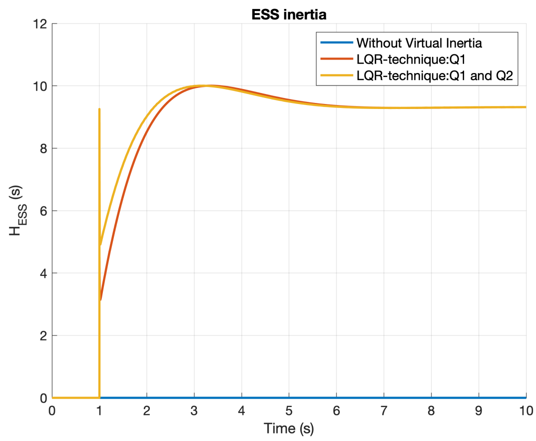

Fig. 26: *ESS inertia for Case 3.*

than that of Subcase 1. This is because the nadir frequency and the RoCoF are reciprocally related. Specifically, it is impossible for the RoCoF to be lower, whereas the nadir frequency remains the same. In realistic systems, the procedure for tuning the weighted parameters should involve adjusting the Q_1 first. Then, if the RoCoF still exceeds, the Q_2 will subsequently be adjusted to meet the standard.

Since the ESS inertia is adaptive and time-varying, it is adjusted after disturbances occur. In a steady state condition, the ESS inertia is meaningless because its power is determined by the multiplication

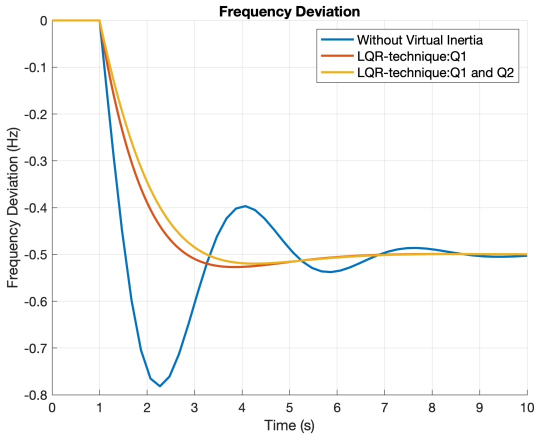

Fig. 27: *Frequency deviation for Case 4.*

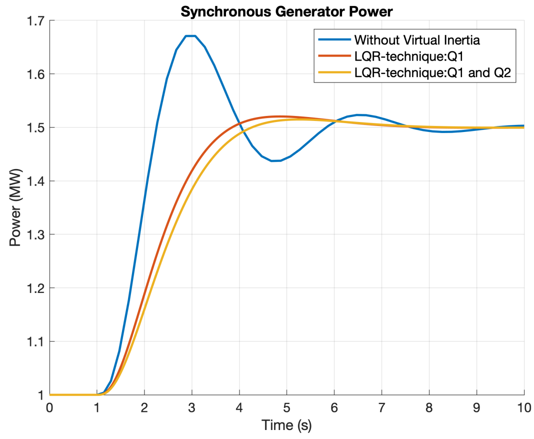

Fig. 30: *SG power #1 and #2 for Case 4.*

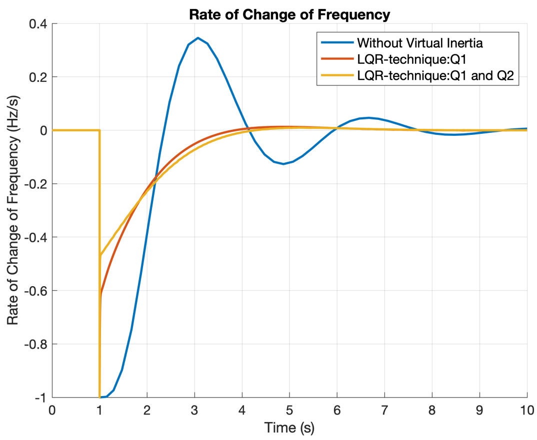

Fig. 28: *RoCoF for Case 4.*

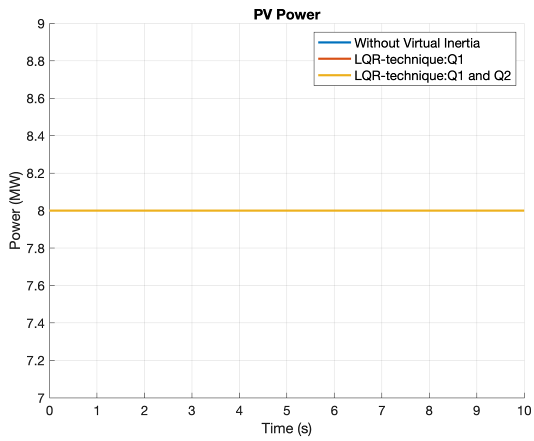

Fig. 31: *PV power for Case 4.*

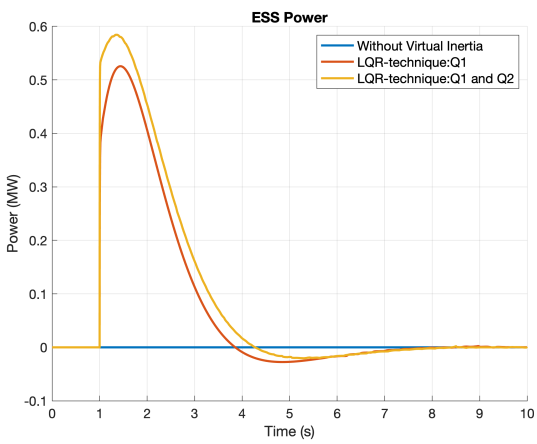

Fig. 29: *ESS power for Case 4.*

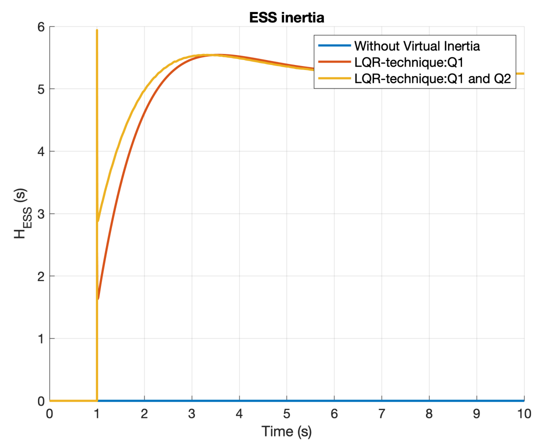

Fig. 32: *ESS inertia for Case 4.*

of RoCoF and ESS inertia. When the RoCoF is zero, the ESS power is also zero, regardless of the existence of ESS inertia. The synchronous generator power in Cases 1–4, during ESS actuation, is less oscillated in comparison to the subcase without ESS inertia. This is another advantage since the physical oscillation of the synchronous generator can be avoided to prevent mechanical damage to the generation unit.

In some small power systems, it is highly possible that once disturbances occur, the frequency deviation might not violate the standard, although the RoCoF is higher than limitation. Therefore, the method

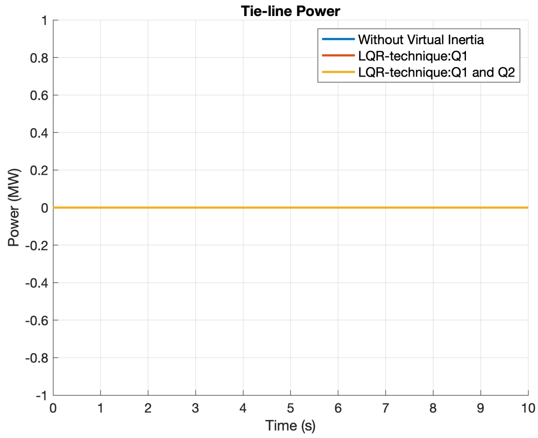

Fig. 33: *Tie-line power for Case 4.*

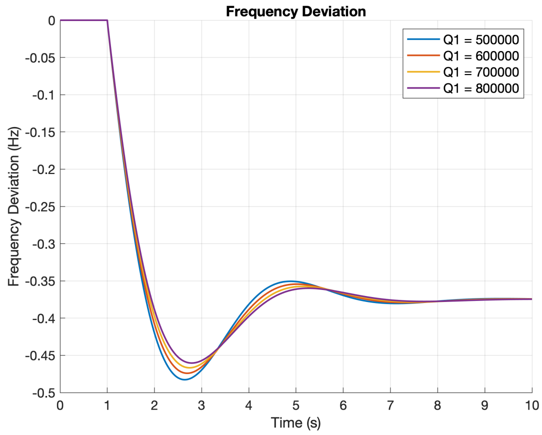

Fig. 34: *Frequency deviation for scenario 1.*

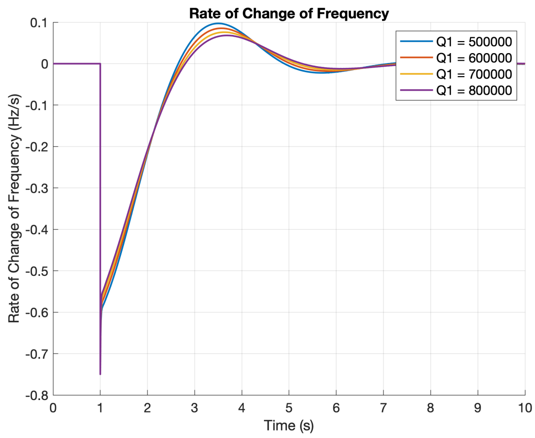

Fig. 35: *RoCoF for scenario 1.*

proposed in this paper is suitable for this kind of power system. This is because the weighted parameters can be freely adjusted, thereby affecting the adaptive inertia. Characteristically, the ESS needs to inject or absorb a considerable amount of power but the amount of energy is rather small. A battery type ESS could be used. According to the results, the minimum size of the ESS for this application would be 604 kW and 14.23 kWh, selected from the maximum values. However, the battery capacity is very small since it is used for only a short time, and can be employed in other applications. The typical rating of a battery energy storage system is around 1 kW–100 MW, which is suitable for the proposed virtual inertia application [24, 25].

7. SENSITIVITY ANALYSIS

In this section, the relationship between the weighted parameters Q_1 and Q_2 and frequency response performance indices (nadir frequency and RoCoF) is investigated. There are two scenarios in this section. In both scenarios, all system parameters are equal to those in Case 1 in Section 5. The disturbance type and severity are also the same as those in Case 1. The only change relates to the weighted parameters Q_1 and Q_2. In scenario 1, the weighted parameter Q_1 increases from 500,000 to 800,000 with an increment of 100,000, but Q_2 is fixed at 1. In scenario 2, the weighted parameter Q_2 increases from 100,000 to 400,000 with an increment of 100,000, but Q_1 is fixed at 1. Figs. 34 and 35 illustrate the frequency deviation and RoCoF for scenario 1, whereas Figs. 36 and 37 illustrate the frequency deviation and RoCoF for scenario 2.

Furthermore, the results illustrate that the ESS controlled by the LQR technique can improve both frequency response performance indices. Since the lower inertia in the microgrid makes the frequency stability more sensitive, it is unclear whether the nadir frequency or the RoCoF violates the grid code first. Another advantage is that the weighted parameters of ESS controlled by the LQR technique could be fine-tuned to make them suitable for each microgrid. Finally, it is apparent from the results that the control performance indices are not coupled, but seem to support in the same direction.

8. CONCLUSION

Since the system inertia tends to be lower due to the higher penetration of PV in the microgrid, the frequency stability seems to deteriorate. The issued frequency response performance indices are nadir and RoCoF. This is because they are critical indices in the frequency protection system, both for synchronous generator protection and stepping load shedding. The ESS is seemingly becoming more popular for solving other problems in the microgrid and could be controlled to have virtual inertia using the LQR technique. Using the proposed procedure—calculating the proper weighted parameters for each system—the microgrid could be guaranteed to maintain frequency stability in the event of an abrupt disturbance while connected to the main grid or operating in the

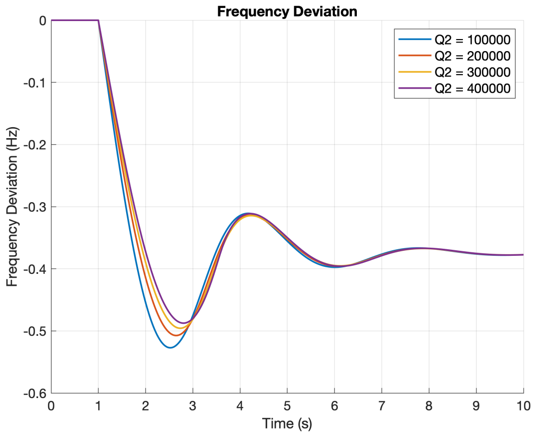

Fig. 36: *Frequency deviation for scenario 2.*

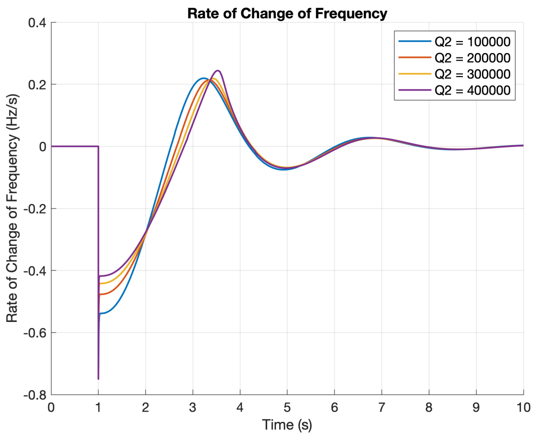

Fig. 37: *RoCoF for scenario 2.*

islanding mode, as demonstrated by the results. Furthermore, another advantage of the proposed procedure is that the weighted parameter could be fine-tuned independently to suit each microgrid identity. According to Bloomberg NEF, the cost of a four-hour duration lithium-ion battery system in 2020 was $320 per kWh, predicted to decrease to $104 per kWh by 2050.

Future work could involve the identification of an algorithm to effectively tune the weighted parameters. Moreover, droop control of inverter-based generation and reactive power management in microgrids should be further investigated.

ACKNOWLEDGMENT

The Crown Prince Maha Vajiralongkorn Scholarship from the Graduate School, Chulalongkorn University, to commemorate the 72nd anniversary of his Majesty King Bhumibala Aduladeja is gratefully acknowledged.

REFERENCES

[1] A. Ulbig, T. S. Borsche, and G. Andersson, “Impact of Low Rotational Inertia on Power System Stability and Operation,” *IFAC Proceedings Volumes*, vol. 47, no. 3, pp. 7290–7297, 2014.

[2] P. G. Bueno, J. C. Hernández, and F. J. Ruiz-Rodriguez, “Stability assessment for transmission systems with large utility-scale photovoltaic units,” *IET Renewable Power Generation*, vol. 10, no. 5, pp. 584–597, May 2016.

[3] Australian Energy Market Operator (AEMO), “National Transmission Network Development Plan,” Dec. 2018. [Online]. Available: `https://www.aemo.com.au/-/media/Files/Electricity/NEM/Planning_and_Forecasting/NTNDP/2018/2018-NTNDP.pdf`

[4] Nahid-Al-Masood, R. Yan, T. K. Saha, and N. Modi, “Frequency response and its enhancement using synchronous condensers in presence of high wind penetration,” in *2015 IEEE Power & Energy Society General Meeting*, 2015.

[5] V. Trovato, I. M. Sanz, B. Chaudhuri, and G. Strbac, “Advanced Control of Thermostatic Loads for Rapid Frequency Response in Great Britain,” *IEEE Transactions on Power Systems*, vol. 32, no. 3, pp. 2106–2117, May 2017.

[6] J. Fang, Y. Tang, H. Li, and X. Li, “A Battery/Ultracapacitor Hybrid Energy Storage System for Implementing the Power Management of Virtual Synchronous Generators,” *IEEE Transactions on Power Electronics*, vol. 33, no. 4, pp. 2820–2824, Apr. 2018.

[7] U. Akram and M. Khalid, “A Coordinated Frequency Regulation Framework Based on Hybrid Battery-Ultracapacitor Energy Storage Technologies,” *IEEE Access*, vol. 6, pp. 7310–7320, 2018.

[8] J. Rocabert, R. Capó-Misut, R. S. Muñoz-Aguilar, J. I. Candela, and P. Rodriguez, “Control of Energy Storage System Integrating Electrochemical Batteries and Supercapacitors for Grid-Connected Applications,” *IEEE Transactions on Industry Applications*, vol. 55, no. 2, pp. 1853–1862, 2019.

[9] V. Knap, R. Sinha, M. Swierczynski, D. Stroe, and S. Chaudhary, “Grid inertial response with Lithium-ion battery energy storage systems,” in *2014 IEEE 23rd International Symposium on Industrial Electronics (ISIE)*, 2014, pp. 1817–1822.

[10] M. Ashabani, F. D. Freijedo, S. Golestan, and J. M. Guerrero, “Inducverters: PLL-Less Converters With Auto-Synchronization and Emulated Inertia Capability,” *IEEE Transactions on Smart Grid*, vol. 7, no. 3, pp. 1660–1674, May 2016.

[11] Q. Zhong and G. Weiss, “Synchronverters: Inverters That Mimic Synchronous Generators,”

IEEE Transactions on Industrial Electronics, vol. 58, no. 4, pp. 1259–1267, April 2011.

[12] Q. Zhong, P. Nguyen, Z. Ma and W. Sheng, "Self-Synchronized Synchronverters: Inverters Without a Dedicated Synchronization Unit," *IEEE Transactions on Power Electronics*, vol. 29, no. 2, pp. 617–630, Feb. 2014.

[13] S. D'Arco and J. A. Suul, "Virtual synchronous machines — Classification of implementations and analysis of equivalence to droop controllers for microgrids," in *2013 IEEE Grenoble Conference*, 2013.

[14] R. Hesse, D. Turschner, and H.-P. Beck, "Micro grid stabilization using the virtual synchronous machine (VISMA)," *Renewable Energy & Power Quality Journal*, vol. 1, no. 7, pp. 676–681, Apr. 2009.

[15] H. Beck and R. Hesse, "Virtual synchronous machine," in *2007 9th International Conference on Electrical Power Quality and Utilisation*, 2007.

[16] Y. Chen, R. Hesse, D. Turschner, and H.-P. Beck, "Comparison of methods for implementing virtual synchronous machine on inverters," *Renewable Energy & Power Quality Journal*, vol. 1, no. 10, pp. 734–739, Apr. 2012.

[17] M. P. N. van Wesenbeeck, S. W. H. de Haan, P. Varela, and K. Visscher, "Grid tied converter with virtual kinetic storage," in *2009 IEEE Bucharest PowerTech*, 2009.

[18] N. Pogaku, M. Prodanovic, and T. C. Green, "Modeling, Analysis and Testing of Autonomous Operation of an Inverter-Based Microgrid," *IEEE Transactions on Power Electronics*, vol. 22, no. 2, pp. 613–625, Mar. 2007.

[19] F. Katiraei and M. R. Iravani, "Power Management Strategies for a Microgrid With Multiple Distributed Generation Units," *IEEE Transactions on Power Systems*, vol. 21, no. 4, pp. 1821–1831, Nov. 2006.

[20] K. Ogata, *Modern Control Engineering*, 5th ed. New Jersey, USA: Prentice Hall, 2010.

[21] Electricity Generating Authority of Thailand (EGAT), "System Performance under Contingency Standard".

[22] S. Curi, D. Groß, and F. Dörfler, "Control of low-inertia power grids: A model reduction approach," in *2017 IEEE 56th Annual Conference on Decision and Control (CDC)*, 2017, pp. 5708–5713.

[23] U. Markovic, Z. Chu, P. Aristidou, and G. Hug, "Fast Frequency Control Scheme through Adaptive Virtual Inertia Emulation," in *2018 IEEE Innovative Smart Grid Technologies - Asia (ISGT Asia)*, 2018, pp. 787–792.

[24] A. Poullikkas, "A comparative overview of large-scale battery systems for electricity storage," *Renewable and Sustainable Energy Reviews*, vol. 27, pp. 778–788, Nov. 2013.

[25] K. Zach, H. Auer, and G. Lettner, "D2.1 Report Summarizing the Current Status, Role and Costs of Energy Storage Technologies", StoRE Project, Dec. 2011. [Online]. Available: `https://www.store-project.eu/documents/results/en_GB/report-summarizing-the-current-status-role-and-costs-of-energy-storage-technologies`

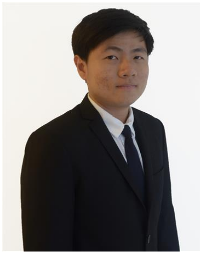

Gorn Suphahathanukul received his B.Eng. degree from King Mongkut's University of Technology Thonburi (KMUTT), Bangkok, Thailand in 2016 and M.Eng. from Chulalongkorn University, Bangkok, Thailand in 2019. He is currently an Adjunct Lecturer at the Department of Electrical Engineering, KMUTT, Bangkok, Thailand. His current research interests include power system dynamics and control, smart grid technologies, renewable energy integration, and railway electrification.

Pisitpol Chirapongsananurak received his B.Eng. and M.Eng. degrees in Electrical Engineering from Chulalongkorn University, Bangkok, Thailand, in 2009 and 2011, respectively, and the Ph.D. degree in Electrical Engineering from The University of Texas at Austin, Austin, TX, USA, in 2016. He was a Research Fellow at The University of Texas at Austin in 2016. He is currently a Lecturer at the Department of Electrical Engineering, Chulalongkorn University, Bangkok, Thailand. His research interests include power quality, power system dynamics and control, power system modeling and simulation, renewable energy integration, and wind and solar power generation.

Naebboon Hoonchareon received his B.Eng. degree in Electrical Engineering from Chulalongkorn University, Bangkok, Thailand, and the MSEE and Ph.D. degrees from Purdue University, Indiana, USA. He has joined Faculty of Engineering, Chulalongkorn University, Bangkok, Thailand since 2002, and now become an Associate Professor at the Department of Electrical Engineering, and head of Smart Grid Research Unit. His research interests are in power system dynamics and control, and energy management systems in smart grid.